Operando X-ray scattering elucidates the photocorrosion mechanism of $CuBi_2O_4$ films

Davide Derelli[#1], Francesco Caddeo[#1], Kilian Frank[2], Kilian Krötzsch[1], Patrick Ewerhardt[1], Marco Krüger[1], Sophie Medicus[1], Lars Klemeyer[1], Marvin Skiba[1,3], Olof Gutowski[4], Ann-Christin Dippel[4], Wolfgang J. Parak[1,3], Bert Nickel[2], Dorota Koziej[1,3*]

[1] University of Hamburg, Institute for Nanostructure and Solid-State Physics, Center for Hybrid Nanostructures, Hamburg, Germany

[2] Ludwig-Maximilians-Universität München, Faculty of Physics and Center for NanoScience (CeNS), Munich, Germany

[3] The Hamburg Centre for Ultrafast Imaging, Hamburg, Germany

[4] Deutsches Elektronen-Synchrotron DESY, Hamburg, Germany

[#]equal contribution

*Corresponding author. email: dorota.koziej@uni-hamburg.de

Keywords: operando X-ray scattering, photocorrosion, water splitting, copper bismuth oxide, thin films,

TOC:

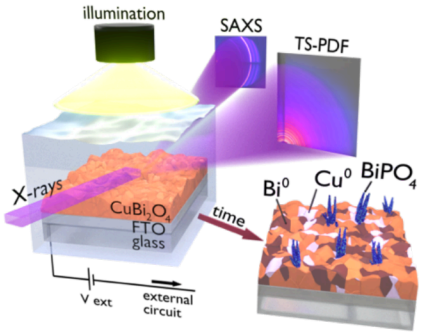

The surface sensitivity of Total Scattering of atomic Pair-Distribution Function (TS-PDF) and Small Angle X-ray Scattering (SAXS) enables studying the interplay between the structural changes and photoelectrochemical performance of photocathodes. $CuBi_2O_4$ undergoes photocorrosion to Bi and Cu, and further dissolves releasing Cu ions in the electrolyte and forming $BiPO_4$. The rapid formation of Bi correlates with an abrupt drop of photocurrents.

ABSTRACT. $CuBi_2O_4$ has recently emerged as a promising photocathode for photo-electrochemical (PEC) water splitting. However, its fast degradation under operation currently poses a limit to its application. Here, we report a novel method to study operando the semiconductor-electrolyte interface during PEC operation by surface-sensitive high-energy X-ray scattering. We find that a fast decrease in the generated photocurrents correlates directly with the formation of a metallic Bi phase. We further show that the slower formation of metallic Cu, as well as the dissolution of the electrode in contact with the electrolyte, further affect the $CuBi_2O_4$ activity and morphology. Our study provides a comprehensive picture of the degradation mechanisms affecting $CuBi_2O_4$ electrodes under operation and poses the methodological basis to investigate the photocorrosion processes affecting a wide range of PEC materials.

Introduction

Photo-electrochemical (PEC) water splitting is currently one of the most promising approaches for the conversion of solar energy into hydrogen gas (H_2), which can be then transported and used on demand as a green energy carrier.[1] In a PEC cell, a semiconductor is immersed in an electrolyte and the charge carriers are generated under light illumination at the semiconductor-electrolyte interface, effectively combining light absorption and catalysis in a single device.[2] One major challenge to this approach is the intrinsic low stability of most semiconductors which rapidly degrade when in contact with the electrolyte during PEC measurements.[3] Common degradation pathways include the dissolution of the photo-absorbing material into the electrolyte, phase transformations due to the reduction/oxidation of the metallic species under applied bias and/or illumination, loss of the semiconductor layer from the electrode surface, and the morphological restructuring of the electrode surface. Such complex degradation mechanisms cause the decline of its PEC performances. For example, Cu_2O photocathodes reduce during operation to the inactive metallic Cu phase and concurrently oxidize to release Cu^{2+} ions into the electrolyte.[4] $BiVO_4$ photoanodes dissolve into stoichiometric Bi and V species leading to a progressively reduced thickness of the photo-absorbing layer,[5] while the surface of metal nitride electrodes passivates due to the formation of a metal oxide layer, which prevents the efficient charge transport at the semiconductor-electrolyte interface.[6]

Understanding the mechanisms underlying photocorrosion constitutes the fundamental prerequisite to improve the durability of PEC electrodes by establishment of appropriate mitigation strategies. Moreover, as there will be a limited lifetime of PEC electrodes, i.e., after operation they will need to be disposed as waste, insights into their degradation on various time scales will enable development of sustainable disposal approaches. The in situ and operando methods hold the promise to provide systematic insights into the photocorrosion phenomena by monitoring the PEC material under relevant timescales and operating conditions, i.e. under applied bias and illumination. So far, techniques such as ambient pressure x-ray photoelectron spectroscopy (APXPS), inductively coupled plasma mass spectroscopy (ICP-MS) and in-situ UV-Vis spectroscopy have been used to assess the photocorrosion mechanism of Cu_2O, WO_3, $BiVO_4$ and n-GaP photoelectrodes under realistic working conditions.[7] Additionally, X-ray absorption (XAS), Fourier-transform infrared (FTIR) and Raman spectroscopies have been used to monitor in-situ/operando the catalytically active sites and reaction intermediates during the oxygen evolution reaction (OER).[8] Aforementioned methods benefit from enhanced surface sensitivity, allowing to monitor the oxidation states of metal ions at the surface of the electrodes and their dissolution into the electrolyte, but they are limited to the determination of the local atomic environment. X-ray scattering, including total scattering with pair distribution function analysis (TS-PDF) and small-angle scattering (SAXS), is sensitive to morphological and structural changes ranging from the atomic up to nanometer length scales. Thus, it permits to probe local atomic structures as well as the restructuring of the electrode surface and the formation of new phases. Yet, the operando X-ray scattering investigations were restricted only to few electrochemical studies,[9] while the technique has never been applied to monitor the surface of photoactive films in a PEC cell.

In this work, we close this gap. We develop an operando grazing-incidence X-ray scattering approach that allows to assess the evolution of structural processes at the surface of a photoactive film in a PEC cell during operation, as shown in **Figure 1a and Figure S1-2**. We use a high-energy X-ray probe and a large-area detector to collect the TS signal at grazing-

incidence angle with enhanced surface sensitivity. Simultaneously, we use a second large-area detector to collect the SAXS signal.

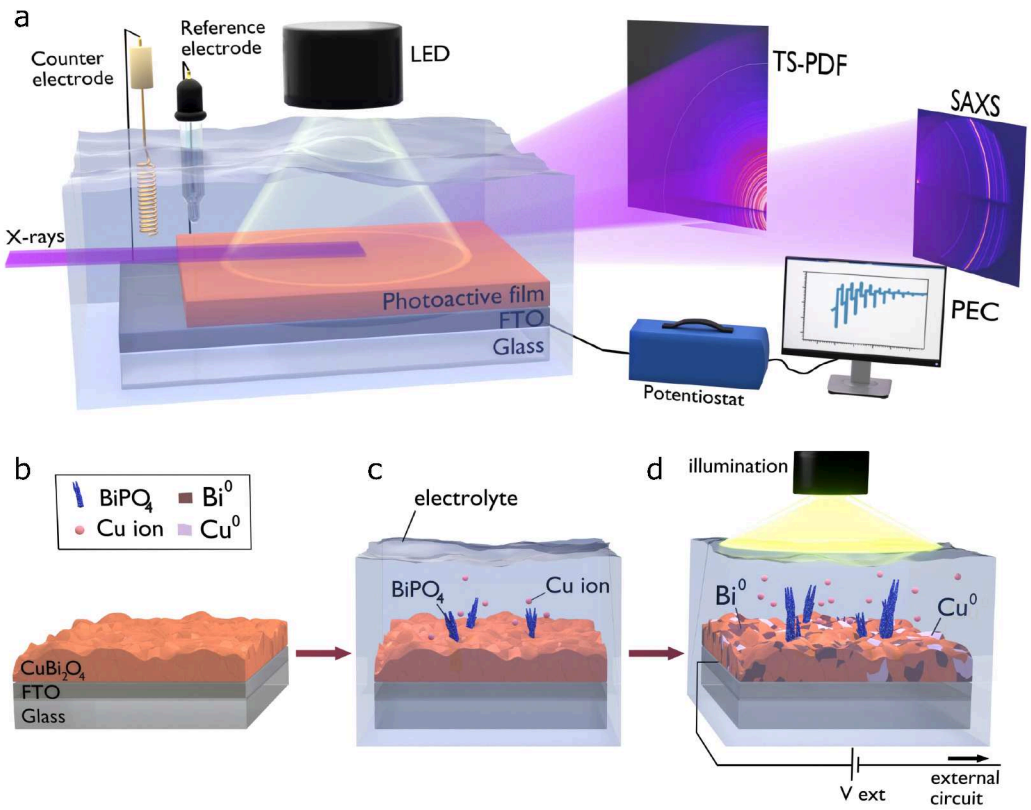

Fig. 1: Overview of the operando photo-electrochemical setup and of the main findings of the present work. a Schematic illustration of the multi-modal experimental setup. Photoelectrochemical (PEC) properties of a photoactive thin film under illumination and immersed in an electrolyte solution are probed by use of a potentiostat in a standard 3-electrode configuration. Two large-area X-ray detectors permit the simultaneous measurement of both TS and SAXS signals from the film surface in a grazing incidence geometry. Schematic drawings of a $CuBi_2O_4$ electrodes **b** and the degradation mechanisms when only immersed in the electrolyte **c,** and under illumination and external bias **d**, respectively.

We apply the technique to monitor operando the structural evolution of a copper bismuth oxide film as a model system. $CuBi_2O_4$ has recently emerged as a promising PEC material due to its favorable electronic properties, namely a suitable bandgap of 1.6-1.8 eV[10], p-type conductivity, and a very cathodic onset potential of ca. 1 V vs. RHE[11] (Reversible Hydrogen Electrode). However, the achievable photocurrents from bare $CuBi_2O_4$ electrodes are limited by the poor charge carrier mobility and the short carrier diffusion length and decay rapidly in steady-state conditions while at the same time no hydrogen is produced,[12] thus indicating that the measured photoactivity likely restrict to a photocorrosion process. It has been suggested that $CuBi_2O_4$ electrodes might degrade similarly to Cu_2O during operation, i.e. via consumption of the photogenerated electrons to the reduction of the Cu^{2+} cations to either Cu^+ or Cu^0.[12] However, this hypothesis lacks of experimental evidence. Here we show that multiple degradation pathways are occurring in parallel at the surface of $CuBi_2O_4$ electrodes. In particular, we find that $CuBi_2O_4$ reduces to metallic Bi and metallic Cu during operation, as shown in **Figure 1b,** while at the same time Cu ions are released in the electrolyte and $BiPO_4$ crystallizes on the electrode surface also in the absence of applied bias and illumination. We

verify our findings by complementary ex-situ X-ray absorption near-edge spectroscopy (XANES), ICP-MS and electron microscopy studies.

Results and Discussion

Morphological and photo-electrochemical characterization of $CuBi_2O_4$ electrodes. In **Figure 2 a, b** we show cross-section and top-view SEM images of the $CuBi_2O_4$ films prepared via spin-coating on fluorine-doped tin oxide (FTO) coated glass substrates. The films display a polycrystalline porous morphology consisting of partially sintered particles of size between 150 to 400 nm forming a reticulated nanostructure, similarly to other $CuBi_2O_4$ films previously reported.[11, 13] The cross-section SEM image in **Figure 2a** shows that the porosity of the film extends throughout all the electrode thickness of ca. 870 nm. In **Figure S3 a**, **b** we also report the UV-visible absorption spectra and the X-ray diffraction (XRD) pattern for the prepared $CuBi_2O_4$ films, which possess a crystalline structure with space group P4/ncc . We first characterized the PEC properties of the $CuBi_2O_4$ films in a commercial cell using a solar simulator as a light source and a sulfate-phosphate electrolyte at pH 5.7, that is a standard in the case of Cu-based photocathodes, which are generally unstable in acidic solutions.[4, 14] In **Figure S4a**, a linear-sweep voltammetry (LSV) scan measured in chopped light displays an on-set potential of 0.95 V vs. RHE and cathodic photocurrents of ca. 200 $\mu A \cdot cm^{-2}$ at 0.3 V vs. RHE, in line with previously reported studies. [11, 13a, 15] In **Figure S4b** we also report the open-circuit potential (OCP) measured under alternating dark and light conditions, which reveals an internal photovoltage of ca. 400 mV. From the Mott-Schottky plot in **Figure S4c** we estimated a flat band potential (φ_{fb}) of 1.20-1.25 V vs. RHE and an acceptor density (N_a) of $8.8 \cdot 10^{18}$ cm^{-3}, in agreement with previously reported values.[11]

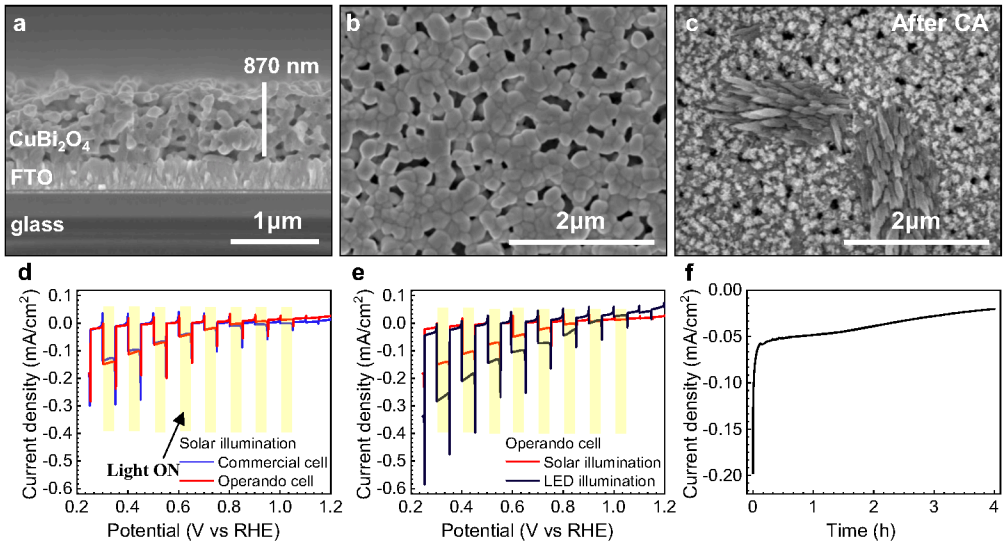

Figure 2: Morphological and photo-electrochemical characterization of $CuBi_2O_4$ film stability. a Cross-section and **b** top-view Scanning Electron Microscopy (SEM) images of the $CuBi_2O_4$ films deposited on a FTO substrate, showing a polycrystalline and porous morphology. **c** SEM image of the $CuBi_2O_4$ surface after 4 hours chronoamperometry (CA) at 0.45 V vs. RHE under illumination, showing morphological changes due to photocorrosion. **d** Chopped-light LSV scans of an individual $CuBi_2O_4$ film performed either in the operando or a commercial PEC cell, using a solar simulator as a light source. **e** LSV scans comparing the photo-electrochemical response of a $CuBi_2O_4$ by using either a solar simulator or a LED light source. **f** Long-term chronoamperometry measured at 0.45 V vs. RHE. All PEC

measurements were done using a 0.5 M Na_2SO_4 and 0.1 M NaH_2PO_4 solution at pH = 5.7 as electrolyte. The yellow stripes span over regions of the LSV collected under illumination.

We additionally carried out a long-term (4 h) chronoamperometry measurement at an applied bias of 0.45 V vs. RHE and under simulated solar emission to assess the photocurrent values in steady-state conditions during operation, **Figure 2f**. The initial photocurrents of ca. 200 $\mu A \cdot cm^{-2}$ rapidly decrease to 50 $\mu A \cdot cm^{-2}$ during the first hour of measurement and then further reduce to 20 $\mu A \cdot cm^{-2}$ within the other 3 hours. The 90% decrease in steady-state photocurrents indicates a photocorrosion process. In **Figure 2c** we also show a scanning electron microscopy (SEM) image of the photoactive film after chronoamperometry. The photocorrosion process largely affects the morphology of the electrode, as we notice the appearance of nanoparticles of high electron-contrast together with the formation of micro-sized branched structures at the surface of the film after 4 h of continuous operation.
Prior to the operando X-ray scattering experiments, we validated that the operando PEC cell for high-energy X-ray scattering allows reliable PEC measurements when compared to a commercial cell for PEC characterization. In **Figure 2d** we show that the chopped-light LSV scans performed in either of the two cells and by use of a simulated solar irradiation result in comparable values of photocurrent densities. However, $CuBi_2O_4$ has a bandgap of 1.6-1,8 eV[10] and thus exhibits a considerably high absorbance in the range from 350 to 600 nm, as shown in the UV-Vis absorption spectra in **Figure S3a**. As the emission of the solar simulator is spread over the entire visible and near-IR spectrum, only part of the irradiated power is effectively absorbed by the electrode. We thus carried out additional PEC experiments using LED illumination with the emission wavelength λ centered at 385 nm (**Figure S2**), which allowed to record higher photocurrents compared to the ones obtained using a solar simulator, as shown in the LSV scan in **Figure 2e** and **Figure S5a**. For our operando experiments we therefore utilized the LED illumination, due to both the compactness of the LED unit and the enhanced photo-response of the $CuBi_2O_4$ films to its radiation compared to the solar emission. In **Figure S5b** we further show that LSVs obtained using LED illumination with a calibrated power of 100 mW/cm^2 display comparable photocurrents independently on the cell used for the PEC measurement.

Structural characterization by surface-sensitive high-energy X-ray scattering. We performed simultaneous TS and SAXS measurements under grazing incidence to characterize the crystalline structure and nanoscale morphology of the $CuBi_2O_4$ films. The details of the beamline setup and data processing for the combined TS-SAXS measurement, the thin film alignment procedure and the experimental determination of incident angle are described in **Figure S6-9** and **Table S2**. An overview of the grazing incidence geometry used to obtain X-ray scattering signal with enhanced surface sensitivity is shown in **Figure 3a**. At the small angles of incidence α_i, typically 0.025°, the vertical size, 3 μm, of the focused beam results in a footprint length of typically ca. 7 mm along the surface, probing a statistically relevant electrode area, all within the active surface. For values of α_i below a critical angle α_c, the penetration depth of the evanescent X-rays in the film is low and the scattering signal originates only from the topmost layer of the photoactive material[16] (**Figure S10**). For $\alpha_i > \alpha_c$ the X-ray penetration depth in the sample quickly increases, as indicated by the occurrence of diffraction peaks from the FTO substrate. Measuring at $\alpha_i < \alpha_c$ is therefore essential to determine structural information limited to the surface of the electrode as shown in **Figure 3b,c**. Here we detect the intensity changes of the $CuBi_2O_4$ and FTO reflections as a function of α_i**.** The critical angle of α_c =0.032° is experimentally determined as the angle at which the

intensity of the $CuBi_2O_4$ (211) reflection is maximized while no signal from the FTO structure is detected.

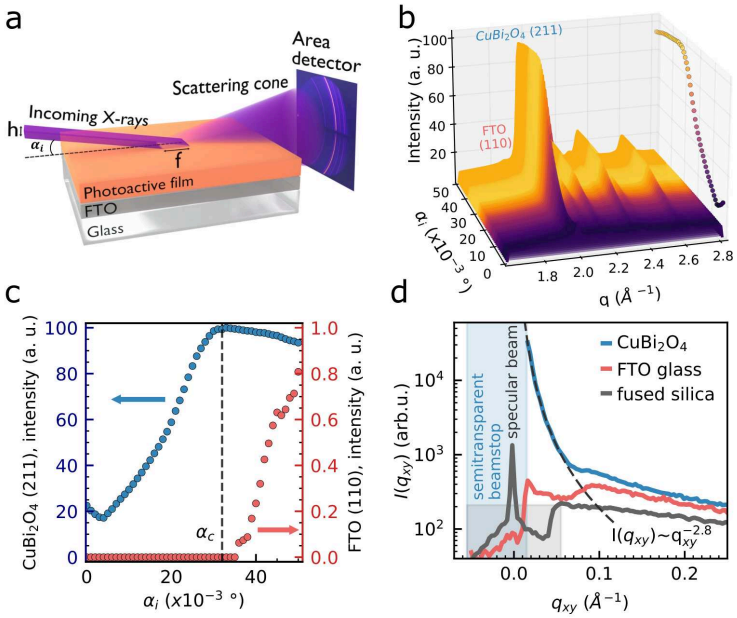

Figure 3: Methodology of high-energy X-ray scattering measurement performed in grazing incidence. a Schematic illustration of the grazing incidence (GI) geometry using a 100 keV X-ray beam focused in one dimension, where h is the vertical beam height, f the X-ray footprint size on the film and α_i is the X-ray incidence angle. **b** Plot of the scattering pattern from a $CuBi_2O_4$ film electrode as a function of the incidence angle α_i. **c** Plots of the peak intensities of the $CuBi_2O_4$(211) and FTO (110) reflections. The dotted vertical line marks the position of the critical angle (**α_c**), above which the scattering signal from the FTO substrate emerges from the background. **d** Plot of the in-plane SAXS intensities of a $CuBi_2O_4$ electrode immersed in the electrolyte under open-circuit conditions compared with an FTO-coated glass slide and a bare fused silica wafer. Part of the signal at low q is weakened by a semitransparent beamstop. A dashed line indicates a $q_{xy}^{-2.8}$ power law identified as the SAXS signal from the porous $CuBi_2O_4$.

Moreover, at a given incidence angle we utilize two large-area detectors positioned at different sample-to-detector (SDD) distances for the acquisition of TS and GISAXS signal at the same time as shown in **Figure S11**. Once the incidence angle is fixed, GISAXS intensities can be extracted from the second detector (**Figure S12**).
Here we report intensity as a function of the scattering vector in the plane of the substrate (q_{xy}) and plot it in **Figure 3d**. In this way, we probe structural features along the electrode-electrolyte interface.[17] The GISAXS intensity from the $CuBi_2O_4$ film is clearly distinguishable and shows a characteristic power law decay $I(q_{xy}) \sim q_{xy}^{-2.8}$ for $0.015 \leq q_{xy} \leq 0.08$ Å^{-1}, i.e. on a length scale ranging between 8 and 40 nm. Such scattering is typical for a porous materials with fractal structure[18] and revealed that the electrode pores reach down to 8 nm in size, i.e. much smaller to what could be determined by simple inspection of SEM micrograph in **Figure 2a**. Furthermore, the GISAXS signal from the reference samples of FTO and bare silica do not display the power law decay observed for the $CuBi_2O_4$ electrode, therefore confirming that the porosity is indeed located in the $CuBi_2O_4$ layer.

Insight into the photodegradation process – ex situ. We measure ex-situ the structural changes of $CuBi_2O_4$ electrodes after photodegradation. To this end, we investigate two

$CuBi_2O_4$ electrodes which were treated with either a 24 h immersion in the electrolyte solution and in the absence of applied bias, or with a 4 h chronoamperometry at 0.5 V vs RHE and under illumination. In **Figure 4a** the respective TS patterns are compared against a pristine $CuBi_2O_4$ film pattern. For the treated electrodes, we observe the emergence of a hydrated crystalline $BiPO_4$ phase (space group $P3_121$), which clearly forms even without applied bias and in the dark by a prolonged immersion of the electrode in the electrolyte. The electrode treated with the chronoamperometry additionally displays intense Bragg's reflections characteristic of metallic Bi (space group R-3m) as well as traces of metallic Cu phase (space group Fm-3m), both as a result of cathodic photocorrosion. This is further supported by X -ray absorption near edge spectroscopy (XANES) at the Cu K-edge of films (**Figure S13) and** inductively coupled plasma mass spectroscopy (ICP-MS) of electrolyte solution **Figure 4b**. The XANES data show the presence of 1.5 % and 12 % of metallic Cu inside the $CuBi_2O_4$ electrode after 40 minutes and 4 hours of chronoamperometry at 0.5 V vs RHE, respectively. The ICP-MS measurements display a steady increase in the concentration of Cu species in solution both, before and during the chronoamperometry. However, no Bi ions could be detected in the electrolyte. While ICP-MS does not provide information over the oxidation state of the detected Cu species, the Pourbaix diagram of Cu indicates that the most stable copper species at the electrolyte pH of 5.7 and the OCP potential of the $CuBi_2O_4$ electrode (~ 0.5V vs. RHE) is Cu^{2+}.[7a] Moreover, SEM/EDX images, **Figure 4c,** clearly show the presence of $BiPO_4$ structures which grows on top of the $CuBi_2O_4$ film as multiple branches, with single branches growing even up to few micrometers in length. **Figure 4d** schematically illustrates both the chemical species and structural modifications detected in electrolyte and at the surface of the electrode as a result of either the reduction or the dissolution of the pristine $CuBi_2O_4$ material under applied external bias and illumination.

Therefore, unlike hypothesized in the literature, our results reveal that the formation of metallic Bi rather than metallic Cu is the most prominent outcome of the photo-electrochemical degradation of $CuBi_2O_4$ by cathodic photocorrosion. However, ex situ characterizations do not reveal the degradation time scales.

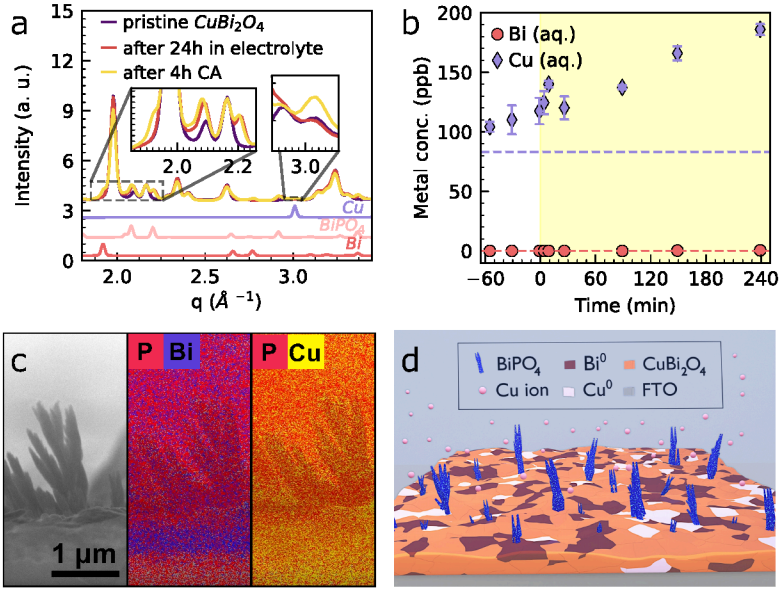

Fig. 4: Degradation of $CuBi_2O_4$ electrode. a Plot of the scattering signal from a pristine $CuBi_2O_4$ electrode (purple) and after either 24h immersion in the electrolyte (red) or 4h CA (yellow). In the inset, zoomed regions of the same plots. **b** Time-resolved plot of the Bi (red circles) and Cu (pink rhombi) ion

content of an electrolyte solution in contact with a $CuBi_2O_4$ electrode as revealed by ICP-MS measurements before and during the CA. Dashed lines indicate the respective ion content determined for the pure electrolyte solution before immersion of the film. The yellow patch highlights the times at which we conducted the chronoamperometric measurement, which was started at time = 0 min. **c** Cross-sectional SEM image of the electrode surface after 4h chronoamperometry. The EDX map for either the P and Bi or P and Cu elements is also shown. **d** Schematic illustration of the morphologies and phases revealed by ex situ TS and SEM-EDX after 4h CA.

Operando structural characterization by X-ray scattering. While the ex-situ characterization permits to identify various changes of the electrode, it is not possible to pinpoint which phenomena are responsible for the abrupt drop in photocurrents within the first minutes of chronoamperometry. For this, we perform time-resolved X-ray scattering and concurrently measure the $CuBi_2O_4$ electrode activity. We record simultaneous TS and SAXS data with an angle of incidence α_i = 0.025°, during chronoamperometry at 0.5 V vs. RHE as shown in **Figure 5a,d.** Under applied illumination and bias, we immediately observe a rapidly decreasing intensity of the reflections characteristic for $CuBi_2O_4$ in the TS signal. Simultaneously, we observe a new feature at q = 1.92 $Å^{-1}$, which corresponds to the (012) reflection of metallic Bi. During the first 40 minutes, we observe neither formation of $BiPO_4$ nor Cu. This is not surprising since the Cu content in the ex situ sample, based on XANES studies shown in **Figure S13**, is only 1.5%, which is below the detection limit of TS. To quantify the respective contribution of the $CuBi_2O_4$ and Bi phases, we Fourier transformed the X-ray total scattering signal into the so-called atomic pair distribution function (PDF, G(r)).[19] We then refine a two-phase structural model of $CuBi_2O_4$ and Bi against the experimental G(r). The background subtraction and PDF modelling and refinement procedures are reported in **Figure S14-17** and **Table S3**. **Figure 5b** shows an example of the two-phase PDF refinement result obtained after 40 minutes of chronoamperometry. The two-phase PDF model with $CuBi_2O_4$ and Bi provides a good fit to the experimental data with R_W of 0.110, and does not indicate the presence of any additional amorphous or locally-ordered structures. We compared the signal from the spot exposed to X-rays during the operando measurement to a previously unexposed spot and observe similar structural changes (**Figure S18)**. Therefore, we can exclude that the Bi formation was induced by the X-ray beam. Interestingly, the appearance of a Bi phase correlates with the decay in measured photocurrent density during the chronoamperometry, as shown in **Figure 5c**. In the first 8 minutes of chronoamperometry, the photocurrent density rapidly decreases by almost one order of magnitude from around -0.20 mA/cm^2 to just -0.03 mA/cm^2. Simultaneously, a reduced Bi phase forms and rapidly grows to constitute 12% of the total detected material. After 30 minutes, the photocurrent density reaches a plateau at -0.015 mA/cm^2 and the fraction of Bi concurrently saturates to 24%.

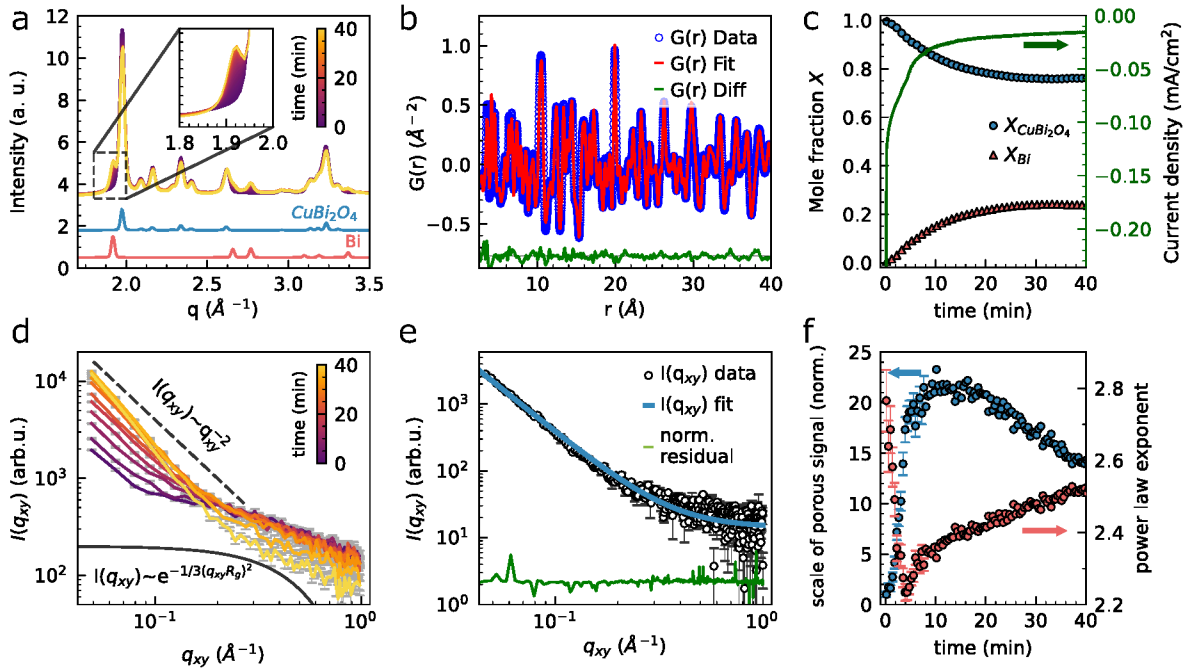

Figure 5: Time-resolved $CuBi_2O_4$ photodegradation studies. a Time-resolved plot of the operando X-ray scattering signal collected from the surface of a $CuBi_2O_4$ electrode under illumination and applied constant bias (0.5 V vs RHE). In the inset, a zoom into the 1.8-2.0 $Å^{-1}$ region highlights the formation of metallic Bi with time. **b** Fit of the operando PDF obtained after 40 min of CA. The fit (red line) of the experimental data (blue circles) was calculated by considering the presence of both a $CuBi_2O_4$ and a Bi phase. The residual between experimental and fit PDF is plotted in green. **c** Evolution of the relative amounts of the $CuBi_2O_4$ (blue circles) and Bi (red triangles) phases during the CA measurement as obtained from the PDF fit. The change in the measured current density over time (green curve) is additionally shown. **d** Time-resolved plot of the operando GISAXS in-plane signal during the CA. The dashed line indicates the power law $q_{xy}^{-2.5}$, while the solid black line shows the Guinier law representing the background signal of small structures (< 0.5 nm) at early times. **e** Fit of the GISAXS in-plane signal obtained after 40 min of CA with a sum of a power law and a Guinier law. The normalized residual is shown in green. **f** Evolution of the GISAXS intensity at $q_{xy,min}$ and the power law exponent during the CA.

In addition to the quantification of the crystalline composition of the film via PDF analysis, we probe the change of nanoscale morphology during chronoamperometry by GISAXS. **Figure 5d** shows the in-plane GISAXS intensity measured between 0 to 40 minutes of CA. We fit the time-resolved intensities with a power law decay to determine changes in the material porosity during operation. We further modelled an additional background arising from small structures (< 0.5 nm) by a Guinier law (**Figure S19-20**). **Figure 5e** shows a representative fit to the data and **Figure 5f** the evolution of structural parameters. In the first 8 minutes of operation the amplitude of the scattering signal ($I(q_{x,y\ min})$) at low-q values quickly increases and reaches a maximum after 20 min, thus indicating that the bulk porosity increases during the initial stage of CA. This result likely comes from the consumption of $CuBi_2O_4$ electrode material and the growth of small metallic Bi deposits. The exponent n of the power law q^{-n}, obtained from the fit, measures the ruggedness or dimensionality of the surface.[18] During the CA, n varies between 2 and 3, which are typical values for non-smooth interfaces probed at low q. After a steeper decline at the beginning of the CA, n slowly increases, indicating that the contribution of compact deposits to the total GISAXS signal

becomes increasingly dominant at intermediate and later stages of the measurement. This behavior likely results from the onset of $BiPO_4$ deposition at the surface of the electrode, which leads to a local increase of the surface compactness. The value of n does not saturate at 40 min, suggesting that the restructuring of the surface may further extend to later times.
We additionally analyze GISAXS data obtained during measurements of the open circuit potential (OCP) under chopped light illumination (**Figures S21-S28**), and account for the transmitted and reflected X-ray intensities by the electrode film. We attribute the dominant change in intensities to a slight, reversible change of incident angle by ±0.0003° upon illumination, while we observe no change in electrode porosity as a result of the OCP measurement.

Discussion of photocorrosion mechanism. Our operando X-ray scattering experiments, together with ex-situ XANES and ICP-MS, allow us to outline the multiple reaction pathways and their respective time scales determining the overall photocorrosion process of $CuBi_2O_4$ films during PEC operation (**Figure 6**).

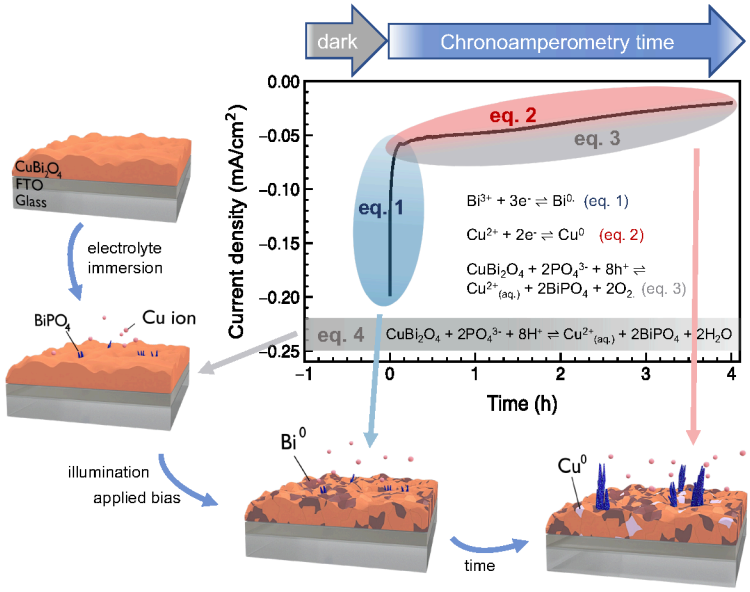

Figure 6: Schematic summary of the multiple reaction pathways and relative time scales determining the degradation of $CuBi_2O_4$ electrodes both before and during the chronoamperometry.

We found that the abrupt drop of the photocurrents occurring during the first few minutes of the chronoamperometric tests (**Figure 2f** and **Figure 5c**) is dominated by the consumption of $CuBi_2O_4$ and the concurrent formation of metallic Bi at the surface of the electrode. This results from a cathodic photocorrosion process, in which the photogenerated electrons are consumed for the reduction of lattice Bi^{3+} ions into Bi^0, which segregates and crystallizes as a metallic Bi phase (eq. 1).

$$\text{cathodic photocorrosion } (\textit{fast}): Bi^{3+} + 3e^- \rightleftharpoons Bi^0 \qquad \text{(eq. 1)}$$
$$(e^- = \text{photogenerated electrons})$$

The quick formation of metallic Bi is not limited by use of a LED illumination but was also determined for a $CuBi_2O_4$ electrodes undergoing chronoamperometry under simulated solar radiation (**Figure S29** and **Table S4**).

The cathodic photocorrosion of Cu^{2+} ions to metallic Cu^0 is also observed, but proceeds at a much slower rate, as evidenced by the ex-situ X-ray scattering and XANES measurements (eq. 2).

$$\text{cathodic photocorrosion (}\textit{slow}\text{):}\quad Cu^{2+} + 2e^- \rightleftharpoons Cu^0 \qquad \text{(eq. 2)}$$

Therefore, we ascribe the fast drop in photocurrents at early stages during the chronoamperometry to the presence of metallic Bi which massively reduces the $CuBi_2O_4$ surface area in direct contact with the electrolyte. Moreover, the absorption properties of the $CuBi_2O_4$ electrode also modify after a short chronoamperometry treatment (**Figure S30**). The ICP-MS investigation, SEM-EDX characterization and ex-situ X-ray scattering reveal the released of Cu^{2+} ions into the electrolyte and the formation of $BiPO_4$ at the surface of the $CuBi_2O_4$ films both in the presence or absence of applied bias and illumination. Under light, these results can be rationalized as outcoming from an anodic photocorrosion process, as photogenerated holes which are not collected at the back contact of the electrode can convert O^{2-} ions from the lattice into O_2 molecules and concurrently release metal ions in the solution (eq. 3). While the Cu^{2+} are effectively released into the electrolyte, the Bi^{3+} cations quickly react at the electrode-electrolyte interface with the solvated PO_4^{3-} anions, determining the formation of $BiPO_4$ crystalline structures.

$$\text{anodic photocorrosion: } CuBi_2O_4 + 8h^+ + 2PO_4^{3-} \rightleftharpoons Cu^{2+}_{(aq.)} + 2BiPO_4 + 2O_2 \qquad \text{(eq. 3)}$$
(h^+ = photogenerated holes)

Although anodic photocorrosion is a common degradation process for n-type semiconductors, it has also been observed for p-type semiconductors of poor hole transport properties,[20] including $CuBi_2O_4$.[21] Finally, the release of Cu^{2+} ions and the formation of $BiPO_4$ in the dark suggests that $CuBi_2O_4$ films are susceptible to dissolve in the electrolyte due to the mildly acidic environment (eq. 4).

$$\text{acidic dissolution: } CuBi_2O_4 + 8H^+ + 2PO_4^{3-} \rightleftharpoons Cu^{2+}_{(aq.)} + 2BiPO_4 + 4H_2O \qquad \text{(eq. 4)}$$

We suggest that the slow formation of $BiPO_4$ structures at the surface of the electrode is mainly responsible for both the decrease in the electrode porosity at later stages of the chronoamperometry and the concurrent decline in the measured photocurrents determined by the growth of an insulating material which effectively screens the $CuBi_2O_4$ surface from the electrolyte, thus reducing the overall electrode activity.

Summary

In this work, we show an operando high-energy X-ray scattering method to investigate the photocorrosion mechanisms and relative time scales on photo-electrochemically active $CuBi_2O_4$ electrodes. We measure TS and SAXS simultaneously in grazing incidence to reveal structural modification close to the $CuBi_2O_4$-electrolyte interface. We show that under illumination and applied bias the $CuBi_2O_4$ electrodes quickly undergo a cathodic photocorrosion process which determines the formation of a segregating metallic Bi phase. This process takes place on a time scale of only few minutes after beginning of the chronoamperometry and correlates with a decrease of around one order of magnitude in the observed photocurrents. Moreover, additional degradation processes occur on slower time

scales: formation of metallic Cu and dissolution in the electrolyte as an effect of both anionic photocorrosion and acidic dissolution. The two phenomena cause a steady release of Cu^{2+} ions in solution as well as the crystallization of $BiPO_4$ branched structures at the surface of the electrode due to the interaction of the releasing Bi^{3+} ions with the phosphate species in the electrolyte. The formation of an insulating $BiPO_4$ layer is likely responsible for the slow decrease in the measured photocurrents at intermediate and later stages of the chronoamperometry.

In summary, our study shows that the high-energy X-ray scattering can probe structural information ranging from atomic to nanometer length scales in a realistic experimental environment, thus allowing to simultaneously correlate chemical and morphological modification of the film electrode with changes of photocurrent. Understanding how photoactive electrodes degrade under operation conditions is the first step towards new strategies for increasing the long-term stability and improving efficiency, but also planning the sustainable disposal strategies. In the future, the developed methodology may find an application in the related fields, where electrolyte/active interface play a crucial role. For example, understanding challenges facing the established Li technology (batteries and capacitor) or emerging technologies like Zn-metal batteries, where dendrite formation still limit their application, or photo-electro-chemical sensing with plasmonic/semiconducting heterostrcutures.[22]

Data Availability

The data that support the findings of this study are openly available in the zenodo repository at http://doi.org/10.5281/zenodo.7997410

Acknowledgements

This work was partially supported by the Bundesministerium für Bildung und Forschung (BMBF) via the project 05K19GU7 / 05K19WMA (LUCENT I) and 05K22GU7 (LUCENT II), Cluster of Excellence "CUI: Advanced Imaging of Matter" of the Deutsche Forschungsgemeinschaft (DFG)−EXC 2056−project ID 390715994, by GRK 2536 NANOHYBRID of the Deutsche Forschungsgemeinschaft, the ERC Consolidator Grant LINCHPIN (grant no. 818941) and the Bavarian State Ministry of Science, Research and Arts through the grant "Solar Technologies go Hybrid (SolTech)".

Parts of this research were carried out at PETRA III at the Deutches Elektronen-Synchrotron DESY (Hamburg, Germany), a member of the Helmholtz Association (HGF) at P07, P21 and P64 beamlines. We greatly thank Dr. Wolfgang Caliebe and Dr. Akhil Tayal for assistance in using beamline P64, and Mr. Stephan Fleig and the team of the Mechanical Workshop (Standortwerkstatt Bahrenfeld) of the University of Hamburg for their help in the realisation of the operando PEC cell.

References

[1] aM. Grätzel, *nature* **2001**, *414*, 338-344; bM. G. Walter, E. L. Warren, J. R. McKone, S. W. Boettcher, Q. Mi, E. A. Santori, N. S. Lewis, *Chemical reviews* **2010**, *110*, 6446-6473; cT. Hisatomi, J. Kubota, K. Domen, *Chemical Society Reviews* **2014**, *43*, 7520-7535; dM. T. Spitler, M. A. Modestino, T. G. Deutsch, C. X. Xiang, J. R. Durrant, D. V.

Esposito, S. Haussener, S. Maldonado, I. D. Sharp, B. A. Parkinson, *Sustainable Energy & Fuels* **2020**, *4*, 985-995.
[2] aO. Khaselev, J. A. Turner, *Science* **1998**, *280*, 425-427; bS. Y. Reece, J. A. Hamel, K. Sung, T. D. Jarvi, A. J. Esswein, J. J. Pijpers, D. G. Nocera, *science* **2011**, *334*, 645-648; cC. Jiang, S. J. Moniz, A. Wang, T. Zhang, J. Tang, *Chemical Society Reviews* **2017**, *46*, 4645-4660; dJ. W. Ager, M. R. Shaner, K. A. Walczak, I. D. Sharp, S. Ardo, *Energy & Environmental Science* **2015**, *8*, 2811-2824.
[3] S. Chen, D. Huang, P. Xu, W. Xue, L. Lei, M. Cheng, R. Wang, X. Liu, R. Deng, *Journal of Materials Chemistry A* **2020**, *8*, 2286-2322.
[4] S. D. Tilley, M. Schreier, J. Azevedo, M. Stefik, M. Graetzel, *Advanced Functional Materials* **2014**, *24*, 303-311.
[5] F. M. Toma, J. K. Cooper, V. Kunzelmann, M. T. McDowell, J. Yu, D. M. Larson, N. J. Borys, C. Abelyan, J. W. Beeman, K. M. Yu, *Nature communications* **2016**, *7*, 12012.
[6] aM. Zhong, T. Hisatomi, Y. Sasaki, S. Suzuki, K. Teshima, M. Nakabayashi, N. Shibata, H. Nishiyama, M. Katayama, T. Yamada, *Angewandte Chemie* **2017**, *129*, 4817-4821; bY. He, J. E. Thorne, C. H. Wu, P. Ma, C. Du, Q. Dong, J. Guo, D. Wang, *Chem* **2016**, *1*, 640-655; cK. Seki, T. Higashi, Y. Kawase, K. Takanabe, K. Domen, *The Journal of Physical Chemistry Letters* **2022**, *13*, 10356-10363.
[7] aG. Liu, F. Zheng, J. Li, G. Zeng, Y. Ye, D. M. Larson, J. Yano, E. J. Crumlin, J. W. Ager, L.-w. Wang, *Nature Energy* **2021**, *6*, 1124-1132; bK. J. Jenewein, A. Kormányos, J. Knöppel, K. J. Mayrhofer, S. Cherevko, *ACS measurement science Au* **2021**, *1*, 74-81; cS. Zhang, M. Rohloff, O. Kasian, A. M. Mingers, K. J. Mayrhofer, A. Fischer, C. Scheu, S. Cherevko, *The Journal of Physical Chemistry C* **2019**, *123*, 23410-23418; dS. Pishgar, J. M. Strain, S. Gulati, G. Sumanasekera, G. Gupta, J. M. Spurgeon, *Journal of Materials Chemistry A* **2019**, *7*, 25377-25388.
[8] aR. Yalavarthi, O. Henrotte, A. Minguzzi, P. Ghigna, D. A. Grave, A. Naldoni, *MRS Energy & Sustainability* **2020**, *7*, E37; bS. Y. Chae, N. Yoon, O. S. Joo, E. D. Park, *Angewandte Chemie* **2023**, *135*, e202215227; cJ. Deng, Q. Zhang, X. Lv, D. Zhang, H. Xu, D. Ma, J. Zhong, *ACS Energy Letters* **2020**, *5*, 975-993; dA. Minguzzi, A. Naldoni, O. Lugaresi, E. Achilli, F. D'Acapito, F. Malara, C. Locatelli, A. Vertova, S. Rondinini, P. Ghigna, *Physical Chemistry Chemical Physics* **2017**, *19*, 5715-5720; eO. Zandi, T. W. Hamann, *Nature chemistry* **2016**, *8*, 778-783.
[9] aS. B. Scott, T. V. Hogg, A. T. Landers, T. Maagaard, E. Bertheussen, J. C. Lin, R. C. Davis, J. W. Beeman, D. Higgins, W. S. Drisdell, *ACS Energy Letters* **2019**, *4*, 803-804; bF. Dionigi, Z. Zeng, I. Sinev, T. Merzdorf, S. Deshpande, M. B. Lopez, S. Kunze, I. Zegkinoglou, H. Sarodnik, D. Fan, *Nature communications* **2020**, *11*, 2522.
[10] N. T. Hahn, V. C. Holmberg, B. A. Korgel, C. B. Mullins, *The Journal of Physical Chemistry C* **2012**, *116*, 6459-6466.
[11] S. P. Berglund, F. F. Abdi, P. Bogdanoff, A. Chemseddine, D. Friedrich, R. van de Krol, *Chemistry of Materials* **2016**, *28*, 4231-4242.
[12] A. Song, I. Levine, R. van de Krol, T. Dittrich, S. P. Berglund, *Chemical Science* **2020**, *11*, 11195-11204.
[13] aI. Rodriguez-Gutierrez, R. Garcia-Rodriguez, M. Rodriguez-Perez, A. Vega-Poot, G. Rodríguez Gattorno, B. A. Parkinson, G. Oskam, *The Journal of Physical Chemistry C* **2018**, *122*, 27169-27179; bZ. Zhang, S. A. Lindley, R. Dhall, K. Bustillo, W. Han, E. Xie, J. K. Cooper, *ACS Applied Energy Materials* **2019**, *2*, 4111-4117.
[14] aJ. Luo, L. Steier, M.-K. Son, M. Schreier, M. T. Mayer, M. Grätzel, *Nano letters* **2016**, *16*, 1848-1857; bL. Pan, J. H. Kim, M. T. Mayer, M.-K. Son, A. Ummadisingu, J. S. Lee, A. Hagfeldt, J. Luo, M. Grätzel, *Nature Catalysis* **2018**, *1*, 412-420.
[15] J. Li, M. Griep, Y. Choi, D. Chu, *Chemical Communications* **2018**, *54*, 3331-3334.
[16] aA.-c. Dippel, M. Roelsgaard, U. Boettger, T. Schneller, O. Gutowski, U. Ruett, International Union of Crystallography, **2019**, pp. 290-298; bA. C. Dippel, O. Gutowski, L. Klemeyer, U. Boettger, F. Berg, T. Schneller, A. Hardtdegen, S. Aussen, S. Hoffmann-Eifert, M. V. Zimmermann, in *Nanoscale, Vol. 12*, **2020**, pp. 13103-13112.
[17] G. Renaud, R. Lazzari, F. Leroy, *Surface Science Reports* **2009**, *64*, 255-380.

[18] D. Mildner, P. Hall, *Journal of Physics D: Applied Physics* **1986**, *19*, 1535.
[19] aT. Egami, S. J. Billinge, *Underneath the Bragg peaks: structural analysis of complex materials*, Elsevier, **2003**; bP. Juhás, T. Davis, C. L. Farrow, S. J. L. Billinge, in *Journal of Applied Crystallography, Vol. 46*, **2013**, pp. 560-566.
[20] H. Gerischer, *Journal of Electroanalytical Chemistry and Interfacial Electrochemistry* **1977**, *82*, 133-143.
[21] D. Kang, J. C. Hill, Y. Park, K.-S. Choi, *Chemistry of Materials* **2016**, *28*, 4331-4340.
[22] aN. S. Choi, Z. Chen, S. A. Freunberger, X. Ji, Y. K. Sun, K. Amine, G. Yushin, L. F. Nazar, J. Cho, P. G. Bruce, *Angewandte Chemie International Edition* **2012**, *51*, 9994-10024; bD. G. Vazquez, T. P. Pollard, J. Mars, J. Yoo, H.-G. Steinrück, S. E. Bone, O. V. Safonova, M. F. Toney, O. Borodin, M. R. Lukatskaya, **2023**; cS. Zhao, M. Riedel, J. Patarroyo, N. Bastus, V. Puntes, Z. Yue, F. Lisdat, W. J. Parak, *Nanoscale* **2021**, *13*, 980-990.